Benjamin J. Colding

Application of a new Biotite-Melt Thermometer to the High-SiO_2 Leucogranite Cap at Spirit Mountain Batholith, NV: Constraints on Temperatures of Melt Segregation

submitted in partial fulfillment of the requirements for the degree of

Master of Science in Earth and Environmental Sciences

Department of Earth and Environmental Sciences

The University of Michigan

Accepted by:

Signature	Name	Date
Robert Holder	Robert Holder	April 7, 2026
Rebecca Lange	Rebecca Lange	April 4, 2026
	Yihe Huang	April 7, 2026
Department Grad Chair Signature	Name	Date

I hereby grant the University of Michigan, its heirs and assigns, the non-exclusive right to reproduce and distribute single copies of my thesis, in whole or in part, in any format. I represent and warrant to the University of Michigan that the thesis is an original work, does not infringe or violate any rights of others, and that I make these grants as the sole owner of the rights to my thesis. I understand that I will not receive royalties for any reproduction of this thesis.

☐ Permission granted.

☐ Permission granted to copy after: _____

☐ Permission declined.

_____

Author Signature

Earth and Environmental Sciences

UNIVERSITY OF MICHIGAN

Abstract

Exposures of voluminous accumulations of high-SiO_2 (>76 wt%) leucogranite (with compositions equivalent to high-SiO_2 rhyolite; HSR) are rare in granitoid bodies at subduction zones yet can be found in regions of continental extension (e.g. Miller et al., 2011). One example is the ~1.5 km thick leucogranite cap (x 25 km) of HSR composition in the Miocene Spirit Mountain batholith in the Colorado River Extensional Corridor, NV. Beneath the leucogranite cap, the Spirit Mountain batholith extends down through ≥4.5 km of granitoid (62-78 wt% SiO_2), where HSR only occurs as localized silicic segregations or as thin aplite dikes (≤ 1 m). At the base of the Spirit Mountain batholith, abundant mafic inclusions occur. Samples from the Spirit Mountain leucogranite cap are compositionally similar to the HSR silicic segregations and aplite dikes found in the underlying granitoid, except for their rare earth element (REE) patterns. The latter display a relative depletion of middle REEs (i.e., horseshoe pattern), reflecting the presence of titanite during melt segregation, whereas the leucogranite cap samples do not show this depletion (i.e., a seagull pattern), consistent with the absence of titanite during melt segregation. In this study, biotite-melt thermometry was applied to 13 samples in the leucogranite cap and 1 sample just below the base of the cap, and the calculated temperatures range from ~786-816°C. These temperatures exceed the thermal stability of titanite of ~760°C, which confirms that temperatures were too hot for titanite to be present during segregation of HSR melts that successfully reached the leucogranite cap, consistent with their seagull REE pattern. These results support the hypothesis that relatively high temperatures are required to segregate HSR under conditions that enable subsequent km-scale transport to form the ~1.5-km thick cap of the Spirit Mountain batholith. Further work is needed to evaluate whether these conditions require a partial melting process, driven by the influx of H_2O-rich fluids from underplated basalts at the

base of the Spirit Mountain batholith. In contrast, there is widespread agreement in the literature that compaction processes during late-stage crystallization of granitoid (at temperatures below the thermal stability of titanite) lead to localized segregations of HSR, which fail to accumulate into significant volumes and/or undergo km-scale transport.

Introduction

High-SiO_2 rhyolite (HSR) is a highly differentiated magma type notable for its low Sr (<50 ppm) and Ba (<200 ppm) concentrations. Because Sr and Ba partition strongly into plagioclase and K-feldspar, respectively, their low concentration values are consistent with its origin as an interstitial melt that segregated from a granitoid mush. However, despite the widespread occurrence of granitoid at subduction zones, HSR is surprisingly rare in volcanic arcs and is only present as thin (typically ≤ 20 cm) aplite dikes in arc-related granitoid belts. The broad failure of HSR to segregate and accumulate to form large plutonic bodies or to erupt in volume at subduction zones may be due to its high viscosity (≥ 10^5 Pa-s) and relatively narrow liquidus-solidus interval (≤50°C; Waters and Andrews, 2016). Despite this, HSR is known to successfully erupt in significant volumes in settings of continental extension, such as the western United States during Cenozoic Basin and Range extension. Quaternary examples of voluminous, caldera-forming HSR eruptions include those at Yellowstone, WY (e.g., Christiansen, 2001) and Long Valley, CA (e.g., Hildreth and Wilson, 2007). Granitoid exposures that reveal significant accumulation of HSR compositions in extensional tectonic settings are rare, but one of the few places they occur is in the Colorado River Extensional Corridor in southern Nevada (**Fig. 1**) where several Miocene bimodal granite-diorite plutons are found. The focus of this study is one of these Miocene plutons, the Spirit Mountain batholith (SMB), which features a ~1.5 km thick

HSR leucogranite cap as part of a >6 km-thick compositionally zoned plutonic body (Walker et al., 2007).

The primary question that is addressed in this study is over what temperature range did HSR melts successfully segregate, undergo transport, and accumulate to form the Spirit Mountain leucogranite (SMLG) cap on top of Spirit Mountain granite (SMG) (**Fig. 2**). Another related question is whether differences in melt segregation temperature explain why some HSR melts reached the SMLG cap, whereas others failed to do so. In this study, a new biotite-melt thermometer, which has been calibrated on both natural HSR samples and phase-equilibrium experiments conducted on HSR starting glass compositions (Gordon et al., in review), is deployed on several samples from the SMLG cap.

The thermometry results may help resolve the cause of a distinct trace-element geochemical difference in HSR samples from the Spirit Mountain batholith, based on data from the literature. HSR samples from the ~1.5 km thick SMLG cap are all characterized by a "seagull" rare-earth element (REE) concentration pattern (**Fig. 3**; Taylor et al., 2025), where all REEs are enriched relative to Eu, which partitions strongly into plagioclase due to its 2+ valence. In contrast, HSR samples in the main ~4.5 km thick SMG unit, found as localized silicic segregations or as aplite dikes, are characterized by a "horseshoe" REE pattern (**Fig. 3**; Taylor et al., 2025), where the middle REEs are depleted relative to the light and heavy REEs. This is the REE pattern found in HSR aplite dikes in granitoid belts at subduction zones (Glazner et al., 2008). It is well understood that the difference between these two REE patterns reflects the absence and presence, respectively, of titanite ($CaTiSiO_5$) in a granitoid mush during HSR melt segregation. Given that titanite has a thermal stability limit of ~760 °C in granitoid systems (Colombini et al., 2011), the hypothesis that is tested in this study is that the HSR samples in the

leucogranite cap all segregated at temperatures hotter than ~760 °C. The biotite-melt thermometry results in this study can then be compared to those obtained on localized HSR segregations inside the SMG unit of the Spirit Mountain batholith (Mack Taylor, personal communication). Together, the temperature data may provide constraints on which process(es) enabled the voluminous accumulation of HSR melt into a ~1.5 km thick cap at the Spirit Mountain batholith when this fails to occur in granitoid batholiths at subduction zones.

Tectonic Setting and Previous Work

The SMB is a ~250 km^2 zoned plutonic body, which has been mapped and sampled on a reconnaissance level by several researchers (Volborth, 1973; Faulds et al., 1992; Hopson et al., 1994; Howard et al., 1994; Haapala et al., 2005; Walker et al., 2007). It is located within the northern Colorado River Extensional Corridor (**Fig. 1**), which underwent lithospheric thinning from ~16-11 Ma (Faulds et al., 1995), in association with Basin and Range extension. The SMB is one of several Miocene bimodal granite-diorite intrusions within the northern Colorado River Extensional Corridor (Miller et al., 2011), and all of them range in age from ~17.5-15.5 Ma and thus overlap the onset of rapid E-W extension (Faulds et al., 2001).

The SMB is the largest of these Miocene intrusions and has undergone 40-50° westward tilting, which has exposed a cross-section from its cap (to the west) down through deep levels of the intrusion (to the east) (**Fig. 2**). Excluding the widespread occurrence of mafic enclaves at the base of the SMB intrusion, it is largely composed of granitoid, ranging from leucogranite at its cap (SMLG), granite in the main body (SMG), and variably exposed quartz monzonite (SMQM) at the base (Walker et al., 2007). The ~1.5 km SMLG cap is exclusively HSR (76-78 wt% SiO_2), and the underlying ~4.5 km thick SMG ranges from ~70-78 wt% SiO_2 (Haapala et al., 2006;

Walker et al., 2007; Taylor and Lange, 2023). The base of the SMB, quartz monzonite, ranges from 62-68 wt% SiO_2 (Haapala et al., 2006; Walker et al., 2007; Taylor and Lange, 2023). The SMQM is dominated by plagioclase and biotite and is relatively depleted in quartz, causing it to be interpreted as a cumulate layer (Walker et al., 2007).

U-Pb zircon geochronology was performed by Walker et al. (2007) on several samples throughout the SMB, which established that it was constructed over a ~2-million-year interval (17.5-15.3 Ma). Evidence of sheet-like intrusions (up to tens of meters thick) is evident in the main SMG unit and the SMLG cap. Evidence of compaction-driven differentiation in the SMG is seen in the occurrence of distinct silicic segregations of HSR composition. The largest of these, that was mapped by Walker et al. (2007), is ~30 m thick and ~120 m wide and is found ~3.5 km below the SMLG cap. Walker et al. (2007), Miller et al. (2011) and Florez et al. (2025) all propose that the primary mechanism enabling segregation of HSR from the main SMG unit in the Spirit Mountain batholith to form the SMLG cap is through compaction during crystallization. In contrast, Taylor et al. (2025) propose that partial melting of the SMG, driven by heat and H_2O-rich fluid from underplated basalts, is the primary mechanism that enabled dike-transport of HSR melt to form the SMLG cap.

Sample Locations and Petrography

The 14 samples used in this study are from a study conducted by Taylor and Lange (2023) and were collected along a power-transmission road on Bureau of Land Management (BLM) land, which traverses the SMLG cap along an E-W transect (**Fig. 2a**). Seven of the 14 samples (SM-69, SM-73, SM-75, SM-80, SM-82, SM-137, SM-175) are host leucogranites with textures that range from phaneritic to hypidiomorphic granular (**Fig. 4a**). An eighth SMLG

sample (SM-174) has a distinctive porphyritic texture in hand sample (i.e., prominent crystals of quartz and K-feldspar) and is part of a sill (identifiable by its porphyritic texture) that is ~22 m thick. A ninth sample (SM-184) is a prominent dike that is ~13 m wide and strikes E-W (vertically above the paleo section of the SMLG cap) and can be traced for >1 km (**Fig. 2b**), and is striking for its porphyritic texture with large prominent crystals of quartz and K-feldspar in a finer-grained matrix **(Fig. 4b).** Four additional samples are relatively thin (≤ 1 m) dikes (compared to SM-184), with widths that overlap the range commonly observed for aplite dikes in granitoid belts. Their widths range from ~22 cm (SM-178), ~60 cm (SM-169) to ~1 m (both SM-171 and 172b). Texturally, in hand sample, these four dikes differ from typical aplite dikes (fine-grained sugary; Glazner et al., 2020) in two ways: (1) their porphyritic character, with prominent quartz and K-feldspar grains, and (2) visible biotite grains **(Fig. 5a),** which are too sparse to see in typical aplite dikes. Finally, one sample (SM-164) is a phaneritic granite from the SMG unit, immediately beneath the SMLG (**Fig. 2**).

Although there is evidence of some chloritization, all 14 samples contain pristine, brown-colored biotite (**Fig. 5b**). The relative abundance of biotite is variable, with some samples containing more (e.g., 5-8% in SM-137) and others containing less (e.g., ~1% in SM-82). In addition to quartz, K-feldspar, plagioclase and biotite, several accessory phases have also been identified in the SMLG samples, including Fe-Ti oxides, titanite, apatite and zircon.

Whole-Rock Geochemistry

Methods

The 14 samples in this study were powdered in a tungsten carbide shatterbox and then analyzed for major and trace elements at Activation Laboratories, Ltd., Ontario, Canada. The

powdered samples were fused into glass beads using lithium metaborate/tetraborate. The beads were then digested in a weak nitric acid solution. Analysis of major elements and select trace elements (e.g., Sr and Ba) was performed by ICP-OES (inductively coupled plasma optical emission spectroscopy). However, analysis of all other trace elements, including rare earth elements, was performed by ICP-MS (inductively coupled mass spectroscopy). Based upon comparisons to standards used by Activation Laboratories and replications, the 1 analytical uncertainty in wt% TiO_2 for these HSR samples is ± 0.01 wt%.

Results

Major-element whole-rock compositions for the 14 samples, normalized to 100% totals, are reported in **Table 1**, together with their original totals and LOI (loss on ignition) values. All samples are high-SiO_2 rhyolites, with 76-79 wt% SiO_2, 0.09-0.14 wt% TiO_2, 11.8-13.4 wt% Al_2O_3, 0.6-1.0 wt% FeO^T, 0.03-0.09 wt% MnO, 0.05-0.17 wt% MgO, 0.3-0.7 wt% CaO, 3.5-4.2 wt% Na_2O and 4.2-5.3 wt% K_2O. Mn/Fe ratios, sometimes used as an index of differentiation (e.g., Li et al., 2020a), range from 0.03-0.13 (**Table 1**). Whole-rock Mg# (=moles MgO/[moles MgO+MnO+ FeO^T]) values range from 13-24%. Select trace element concentrations are also shown in **Table 1**. The SMG sample (SM-164) has the lowest SiO_2 (76.0 wt%) and highest Sr and Ba concentrations (91 and 212 ppm, respectively), but it has a high-SiO_2 rhyolite composition. Among the 13 SMLG samples, Sr varies from 7-59 ppm (11 of 13 samples contain ≤ 23 ppm), and Ba varies from 27-171 ppm (11 of 13 samples contain ≤ 72 ppm). Among the SMLG samples, there is an inverse correlation between Mn/Fe and Sr and Ba, respectively (**Fig. 6**), consistent with elevated Mn/Fe ratios as a sign of differentiation (Li et al., 2020a). Overall, the whole-rock analyses show that all 13 of the SMLG samples are strongly differentiated HSR

compositions. Neither the wide (~13 m) dike sample (SM-184) nor the four thinner (≤ 1 m) dike samples (SM-169, SM-171, SM-172, SM-178) are compositionally distinct from the other eight SMLG samples.

Biotite Compositions

Methods

For all 14 samples, analyses of unaltered biotite crystals in thin sections were obtained with a Cameca SX-100 Electron Microprobe at the University of Michigan. For two samples (SM-164 and SM-184), two thin sections were cut from different parts of each rock sample. The goal was to evaluate compositional heterogeneity among biotite crystals in a hand sample. Analyses were made with a defocused beam (2-5 m), an acceleration voltage of 15 kV, and a beam current of 20 nA. The mineral standards used for each element are presented in **Supplementary Table S1** and are part of the University of Michigan collection. Ten elements were analyzed (Si, Ti, Al, Fe, Mn, Mg, Ba, Ca, Na, and K) with peak and background count times of 20 s, except for Fe (10 s) and Ba (30 s). The average 3 uncertainties on the oxide components, based on counting statistics, are 0.54 wt% for SiO_2, 0.07 wt% for TiO_2, 0.49 wt% for FeO^T, 0.07 wt% for MnO, 0.22 wt% for MgO, 0.07 wt% for BaO, 0.09 wt% for CaO, 0.04 wt% for Na_2O and 0.33 wt% for K_2O. Only analyses with original totals ≥ 94 wt % (prior to biotite formula calculations) were considered successful. Back-scattered electron (BSE) images were taken of all analyzed biotite crystals.

Results

Individual analyses of biotite crystals (≥ 94 wt% totals) obtained for the 14 samples (two samples in duplicate) are tabulated in **Supplementary Table S2**. The average biotite

composition in each thin section is provided in **Table 2**. For each average composition, the number of biotite crystals that were analyzed (N) and the total number of analyses (n) are reported. Note that for some samples, N and n are large (e.g., SM-137, SM-164, and SM-171) due to the abundance of biotite in these samples (5-8%), whereas for other samples, N and n are low (e.g., SM-82), due to the scarcity of biotite in this sample (~1%). It is notable that the samples with the highest abundance of biotite also have the highest whole-rock TiO_2 and MgO contents relative to the other samples.

The average biotite composition for all samples in **Table 2** ranges from 36-40 wt% SiO_2, 1.4-3.2 wt% TiO_2, and 9.0-10.3 wt% K_2O. It is notable that MnO contents are high and range from 0.8-3.3 wt%. The biotite Mg# (=moles MgO/[moles MgO+MnO+ FeO^T]) values range from 40-66%. The model of Li et al. (2020b) was used to calculate the biotite formula from each average composition. The results, also shown in **Table 2**, provide supporting evidence that the biotite analyses are accurate, consistent with their pristine character. Calculated H_2O contents range from 2.6-3.0 wt%, which are maximum values since direct analyses of F and Cl were not obtained. Calculated ferric and ferrous iron concentrations lead to Fe^{3+}/Fe^T values that range from 20-42%. Representative BSE images of biotite are shown in **Fig. 7.**

Some analyses were obtained on chloritized biotite. They are readily identified by their low totals (84-87 %), due to their high-water contents (>13 wt%), and low K_2O contents (0.1-0.7 wt%). Representative analyses are reported in **Supplementary Table S3**. None of the analyses of chloritized biotite were used in this study.

Application of Biotite-Melt Thermometry

Methods

The biotite thermometer that is used in this study is one that is based on the partitioning of TiO_2 between biotite and melt (), and it has been specifically calibrated on high-SiO_2 rhyolites (Gordon et al., in review). A strong correlation between and temperature (~700-800°C) obtained by Fe-Ti oxide thermometry was observed by Jolles and Lange (2019) for a suite of single-clast pumice samples of HSR (≥ 75 wt%) composition from the Bishop Tuff, CA. Gordon et al. (in review) added data and Fe-Ti oxide temperature results from Glass Mountain rhyolites (≥ 76 wt% SiO_2), precursors to the Long Valley caldera-forming eruption that produced the Bishop Tuff, to extend the linear correlation to lower temperatures (716-660°C). They then identified the only published phase-equilibrium experiments conducted on HSR starting glass where biotite was analyzed in the run products (Bolte et al., 2015). These experiments were conducted from 800-825°C and 200 MPa (H_2O fluid saturated) on glass fused from the Blacktail Creek Tuff from the Heise volcanic field, Yellowstone hotspot system. Gordon et al. (in review) obtained values from reported analyses of biotite and glass in the Bolte et al. (2015) run products and plotted the results against experimental temperatures to show that they fall along the same trend line as the natural samples from Long Valley, CA (**Fig. 8**). Gordon et al. (in review) proceeded to conduct several additional hydrous phase-equilibrium experiments on two starting high-SiO_2 rhyolite (≥ 76 wt%) glasses (BT3B and MC24) with differing initial TiO_2 concentrations (0.22 and 0.07 wt%, respectively). The results from their biotite-bearing experimental runs are plotted in **Fig. 8** and confirm the strong linear correlation provided by the natural data. A linear fit (R^2=0.90) to the combined natural and experimental data in **Fig. 8** was performed by Gordon et al. (in review)

and forms the basis of their new biotite-melt thermometer that can be applied to high-SiO_2 rhyolites:

$$T(°C) = 846\ (\pm 6) - 2.31\ (\pm 0.14)* \quad (1)$$

Results

The thermometer in **Eq. 1** can be used to calculate the temperature of biotite crystallization in the SMLG samples from this study because their compositional range overlaps that of all the data used to calibrate **Eq. 1.** To calculate temperature, the value of must be determined for each sample. Since biotite crystallizes close to the liquidus of HSR under hydrous conditions (e.g., Waters and Andrews, 2016), values for the SMLG samples are based upon the ratio of wt% TiO_2 in biotite (**Table 2**) over the wt% TiO_2 in the whole-rock composition (**Table 1**). In other words, the assumption made in this study is that biotite was one of the first phases to crystallize from a liquid composition that matches that of each whole-rock sample. This is the same assumption that was applied to the natural samples (Bishop Tuff and Glass Mountain) in constructing their values shown in **Fig. 8.**

The resulting ratios are reported in **Table 3**, along with propagated 1 errors from the analysis of TiO_2 in biotite (**Table 2**) and in the whole-rock (± 0.01 wt%). values (based on the average biotite composition in each sample) range from 12.5-25.6, with 1 uncertainties that range from ± 1.8-5.0.

The temperatures calculated for the Spirit Mountain samples, using Eq. 1 from Gordon et al. (in review), range from 786-816°C. There are two primary sources of error in these temperatures: (1) the uncertainty in and (2) the uncertainty in the model. In **Table 3**, the 1 propagated error from these two sources on the calculated temperature for each sample is shown,

and ranges from ± 8-13 °C. Duplicate thin sections, and thus two average biotite compositions, were obtained for two samples (Table 2), and the resulting two temperatures (Table 3) overlap within the ± 1 uncertainty for both samples (803 ± 12 °C vs 811 ± 10 °C for SM-164; 787 ± 9 °C vs 790 ± 9 °C for SM-184).

Part of uncertainty in obtained for each sample is due to the variation in TiO_2 content among all the biotite crystals analyzed in each sample (**Table S2**). The 3 standard error of the average TiO_2 content for all analyzed biotite grains in each sample is reported in Table 3, and ranges from 0.36 – 1.71 wt%. Because this exceeds the analytical uncertainty of the microprobe analysis of TiO_2 in biotite due to counting statistics (± 0.07 wt%), it likely reflects the real variation in biotite TiO_2 content for each sample. If it is assumed that the TiO_2 variation in biotite in each sample is caused solely by changes in temperature, the magnitude of this change can be calculated. In **Table 3**, the propagated variation in due to the 3 variation in the TiO_2 content of biotite in each sample is shown, along with the calculated variation in temperature. The calculated temperature intervals in each sample range from 9-31 °C and may represent the cooling interval over which biotite crystallized in the SMLG melts. It is noteworthy that the variation in the TiO_2 concentration within an individual biotite grain can closely match that seen among all the biotite crystals in a sample. An example is one of the biotite crystals from SM-80 (**Fig. 9**) with TiO_2 ranging from 1.44-2.21 wt%, which possibly reflects a temperature variation of ~19°C (808-789 °C) in a sample where all analyzed biotite crystals may collectively record a ~24°C cooling interval (Table 3). Interestingly, the TiO_2 variation in the biotite crystal in Figure 9 does not show a clear core-rim zonation pattern.

In the analysis of above, no variation in the wt% TiO_2 content in the melt phase was considered. The main reason this assumption can be made is that the activity of TiO_2 in a natural

HSR melt is buffered due to co-crystallization of titanomagnetite and ilmenite, which are both near-liquidus phases with biotite in HSR melts. As discussed by Ghiorso and Gualda (2013), the relevant reaction is:

$$Fe_2TiO_4 \text{ (titanomagnetite)} + TiO_2 \text{ (liquid)} = 2FeTiO_3 \text{ (ilmenite)}. \quad (2)$$

Therefore, the initial activity of TiO_2 in the melt at the liquidus is not expected to change during crystallization. The relationship in Eq. 2 allows the TiO_2 concentration in the whole rock melt composition, if assumed to represent the initial liquid composition, to be used for all biotite compositions when constructing values. It may further explain why the natural data in **Fig. 8** are fitted by the linear relationship so well, despite wide variations in the overall degree of crystallization in each sample (1-23%; Jolles and Lange, 2019; Gordon et al., in review).

Discussion

Temperatures of the SMLG cap HSR magmas and the stability of titanite

The thermometry results in **Table 3** provide the average temperature of biotite crystallization in each SMLG sample (two samples in duplicate), as well as the possible temperature interval over which biotite crystallized. These temperatures are plotted relative to the thermal stability limit of titanite in **Fig. 10**, and they exceed 760°C in all cases, even when the full temperature interval of biotite crystallization is considered. Since some cooling is expected during transport after melt segregation, the thermometry data clearly support the hypothesis that all SMLG samples in this study segregated as melts from their granitic source at temperatures too high for titanite to be present. The absence of titanite at the time of melt segregation explains why none of the HSR leucogranite samples from this study show a depletion in their middle REE pattern (i.e., none have a “horseshoe” REE pattern) and instead

show a “seagull” REE pattern (**Fig. 3).** Without titanite present to strongly partition the middle REEs out of the melt, these elements would behave incompatibly with respect to other mineral phases in the granitoid mush (i.e., quartz, K-feldspar, plagioclase, biotite, Fe-Ti oxides, apatite, zircon) and partition preferentially into the melt, producing the “seagull” REE pattern.

A further test of this hypothesis would be to apply biotite-melt thermometry to the HSR silicic segregations within the main granite body (SMG unit) of the Spirit Mountain batholith, all of which feature the REE “horseshoe” pattern (**Fig. 3**). Mack Taylor (personal communication) has performed this additional test (i.e., biotite-melt thermometry). In all four cases, biotite-melt temperatures are colder than the titanite stability limit (Mack Taylor, personal communication). These silicic segregations also have significantly lower concentrations of high-field strength elements (e.g., Hf, Nb and Ta), which strongly partition into titanite (e.g., Olin and Wolff, 2012), relative to the SMLG samples. Therefore, the hypothesis that segregated HSR melts that failed to escape the main granite zone of the SMB did so at temperatures systematically colder than those HSR melts that underwent successful transport to the leucogranite cap is additionally supported.

Constraints on mechanism of segregation and transport of HSR melts that formed the SMLG cap

The thermometry results of this study, together with those from Mack Taylor (personal communication), have implications for the mechanism(s) by which HSR melt is segregated from and transported out of granitic mushes. An outstanding question is what enables segregated HSR melt to undergo km-scale transport and accumulate in large volume in some cases (e.g., the ~1.5 km thick SMLG; **Fig. 2a**), and why it fails to do so in other cases (e.g., the silicic segregations and aplite dikes in the SMG; **Fig. 2**). The biotite-melt thermometry results applied to the SMLG samples from this study suggest that temperature is a factor.

Several researchers who have studied the SMB (e.g., Walker et al., 2007; Miller et al., 2011; Florez et al., 2025) emphasize the role of compaction in a crystal-rich mush to drive segregation of interstitial HSR melts to produce the ~1.5 km-thick SMLG cap. Although compaction during crystallization of the main granite body (SMG unit; **Fig. 2a**) was undoubtedly an important process that led to the localized silicic segregations of HSR in the SMG, it is unclear if it was also the process that led to the thick SMLG cap. When melt ascends during the compaction processes, it does so by buoyant ascent along crystalline grain boundaries. In order for this process to lead to the formation of the SMLG cap, a mushy column of granite containing interstitial melt must be continuously present up to the SMLG cap layer. Although this may have been plausible during the early stages of SMB assembly when the intrusion was thin, this appears to be unlikely after the SMG unit reached thicknesses >2-5 km since this would require interstitial melt to be present throughout the entire SMG unit. Sustaining the elevated temperatures to maintain a long-lived (~2 Myr; Walker et al., 2007) granitoid mush of 2-5 km thickness would require a substantial and sustained influx of basalt at the base (several kms thickness (Calogero et al., 2020), which is not observed.

Instead, the presence of the SM-184 dike (13 m thick) underscores the importance of dike transport of HSR melt into the SMLG layer. A dike of this thickness cannot readily form from interstitial melt in a granitic mush (e.g., Rubin, 1995), and instead only relatively thin, aplite dikes form during late-stage crystallization when the host granitoid can sustain tensile cracks (Glazner et al., 2020). Moreover, km-scale dike transport requires that the surrounding crust be sub solidus, because if the molten HSR dike is intercepted by a granitic mush zone, it would be unable to continue upward to the SMLG cap.

Taylor et al. (2025) agree that compaction during crystallization played an important role in creating the localized HSR segregations found in the SMG zone of the SMB. However, they propose an alternative model to explain the formation and transport of the HSR melt that reached the SMLG cap. Specifically, Taylor et al. (2025) propose that episodic partial melting of the SMG at its base, driven by the influx of hot, H_2O-rich fluids from underplated basalts played a key role. They further explore the role pre-existing aplite dikes during partial melting of the granitoid host. These eutectic HSR aplite dikes would have melted completely when the host granitoid was only partially molten (with titanite melted out). The initial ascent of the aplite dikes would have efficiently drawn the partial melt out of the host granite. The granitoid left behind, depleted in HSR melt, would then form the SMQM unit. This model originated with, and is being fully evaluated by, Mack Taylor (personal communication) as part of his Ph.D. dissertation.

Origin of the unusually high MnO contents in biotite from the HSR leucogranite cap

One of the most striking features of the biotite crystals in the samples from this study is their remarkably high MnO contents (0.8-4.57 wt%). A review of the literature shows that elevated MnO contents in biotite in leucogranites are generally due to elevated Mn/Fe ratios in the melt from which they crystallized (e.g., Li et al., 2020a). A plot of Mn/Fe in biotite vs Mn/Fe in the whole rock for the SMLG samples from this study shows a strong (R^2=0.83) positive linear correlation (**Fig. 11**). These data show that the elevated Mn contents in the SMLG biotite crystals are largely due to the elevated Mn/Fe in their whole-rock compositions and thus reflects their highly differentiated character.

Conclusions

There are several key conclusions that can be derived from this study. First, all analyzed samples from the SMLG cap are biotite-bearing high-SiO_2 rhyolites, irrespective of whether they are phaneritic granitoids or porphyritic dikes. Second, despite the Miocene age of the Spirit Mountain batholith, biotite crystals in the SMLG samples are largely pristine and only a small minority have undergone alteration to chlorite. Third, the elevated MnO contents in the biotite crystals in the SMLG samples reflects the high Mn/Fe ratios in the melts from which they crystallized. Fourth, application of a new biotite-melt thermometer (Gordon et al., in review) to the 14 SMLG samples in this study leads to calculated temperatures that range from 786-816°C, which are above the thermal stability limit of titanite (~760°C; Colombini et al., 2011). This supports the hypothesis that during segregation of the SMLG melts from their granitic source rocks, temperatures were too hot for titanite to be present. Fifth, the absence of titanite during melt segregation of the SMLG samples explains why they do not have the horseshoe REE pattern, which is caused by titanite preferentially partitioning the middle REEs. Instead, the SMLG samples have the seagull REE pattern, consistent with the absence of titanite during melt segregation. These results on HSR samples from the SMLG cap can be compared to those in progress (Mack Taylor, personal communication) on HSR samples from localized segregations within the main SMG unit of the Spirit Mountain batholith to better understand the mechanisms that enable melt segregation followed by km-scale transport of voluminous HSR in some cases (e.g., the SMLG cap), but not others (e.g., localized silicic segregations in the SMG).

References

Bolte T., Holtz F., Almeev R., Nash B. (2015) The Blacktail Creet Tuff: An analytical and experimental study of rhyolites from the Heise volcanic field, Yellowstone hotspot system. Contrib Mineral Petrol 169(2):1-24

Christiansen R. (2001) The Quaternary and Pliocene Yellowstone Plateau volcanic field of Wyoming, Idaho, and Montana. No. 729. US Department of the Interior, US Geological Survey, Professional Paper 729-G, 145 p.

Colombini L., Miller C., Gualda G., Wooden J., Miller J. (2011) Sphene and zircon in the Highland Range volcanic sequence (Miocene, southern Nevada, USA): elemental partitioning, phase relations, and influence on evolution of silicic magma. Mineralogy and Petrology 102(1), 29.

Faulds J., Geissman J., Shafiqullah M. (1992) Implications of paleomagnetic data on Miocene extension near a major accommodation zone in the Basin and Range province, northwestern Arizona and southern Nevada. Tectonics 11(2): 204-227.

Faulds J., Feuerbach D., Reagan M., Metcalf R., Gans, P., Walker, J. (1995) The Mount Perkins block, northwestern Arizona: An exposed cross section of an evolving, preextensional to synextensional magmatic system. Journal of Geophysical Research: Solid Earth 100(B8), 15,249–15,266.

Faulds J., Feuerbach D., Miller C., Smith E. (2001) Cenozoic Evolution of the Northern Colorado River Extensional Corridor, Southern Nevada and Northwest Arizona. The Geologic Transition, High Plateaus to Great Basin - A Symposium and Field Guide (The Mackin Volume): 239-271

Florez D., Huber C., Bachmann O., Sigworth A., Clairborne L., Miller C. (2025) Repacking-driven compaction in the Spirit Mountain batholith, southern Nevada. Journal of Petrology 66(2): egaf003.

Ghiorso M., Gualda G. (2013) A method for estimating the activity of titania in magmatic liquids from the compositions of coexisting rhombohedral and cubic iron-titanium oxides. Contributions to Mineralogy and Petrology 165(1):73-81

Glazner A., Bartley J., Coleman D., Lindgren K. (2020) Aplite diking and infiltration: A differentiation mechanism restricted to plutonic rocks. Contributions to Mineralogy and Petrology 175(4): 37.

Gordon B., Waters L., Lange R. (in review) A new biotite-melt thermometer applicable to high-SiO_2 rhyolites. American Mineralogist.

Haapala I., Rämö O., Frindt S. (2005) Comparison of Proterozoic and Phanerozoic rift related basaltic–granitic magmatism. Lithos 80(1-4), 1–32.

Hopson C., Gans P., Baer E., Blythe A., Calvert A., Pinnow J. (1994) Spirit Mountain Pluton, Southern Nevada: a progress report. Geological Society of America, Abstracts with Programs 26, 60.

Howard K., John B. (1987) Crustal extension along a rooted system of imbricate low-angle faults; Colorado River extensional corridor, California and Arizona. Geological Society of London: Geological Society Special Publications. 28(1):299–311.

Jolles J., SR, Lange R. (2019) High-resolution Fe–Ti oxide thermometry applied to single-clast pumices from the Bishop Tuff: a re-examination of compositional variations in phenocryst phases with temperature. Contributions to Mineralogy and Petrology 174(8): 70.

Li J., Fan W., Zhang L., Ding L., Yue Y., Xie J., Cai F., Quan Q., Sein K. (2020a) Biotite geochemistry deciphers magma evolution of Sn-bearing granite, southern Myanmar. Ore Geology Reviews 121: 103565.

Li X., Zhang C., Behrens H., Holtz F. (2020b) Calculating biotite formula from electron microprobe analysis data using a machine learning method based on principal components regression. Lithos 356: 105371

Miller C., Furbish D., Walker B., Clairborne L., Koteas G., Bleick H., Miller J. (2011) Growth of plutons by incremental emplacement of sheets in crystal-rich host: Evidence from Miocene intrusions of the Colorado River region, Nevada, USA. Tectonophysics 500(1-4): 65-77.

Olin, P.H., Wolff, J.A. (2012) Partitioning of rare earth elements and high-field strength elements between titanite and phonolitic liquid. Lithos 128-131: 46-54.

Rubin A. (1995) Getting granite dikes out of the source region. Journal of Geophysical Research: Solid Earth 100(B4): 5911-5929.

Taylor M., Lange R. (2023) The role of dike transport during differentiation and segregation of a 2-km high-SiO_2 (>76 wt%) leucogranite cap in the zoned Spirit Mountain granite, southern Nevada. Hutton Symposium, Baveno, Italy, program with abstracts.

Taylor M., Colding B., Lange R. (2025) The Failed Supervolcano Spirit Mountain (Avi Kwa Ame): The Critical Role of Basalt and Pre-existing Aplite Dikes in Producing Eruptible High-SiO_2 Rhyolite. American Geophysical Union, New Orleans, LA, program with abstracts.

Volborth A. (1973) Geology of the granite complex of the Eldorado, Newberry, and northern Dead Mountains, Clark County, Nevada. Mackay School of Mines, University of Nevada. 80

Walker Jr B., Miller C., Clairborne L., Wooden J., Miller J. (2007) Geology and geochronology of the Spirit Mountain batholith, southern Nevada: Implications for timescales and physical processes of batholith construction, Journal of Volcanology and Geothermal Research 167, (1–4):239-262

Waters L., Andrews B. (2016) The role of superheating in the formation of Glass Mountain obsidians (Long Valley, CA) inferred through crystallization of sanidine. Contributions to Mineralogy and Petrology 171(10): 79

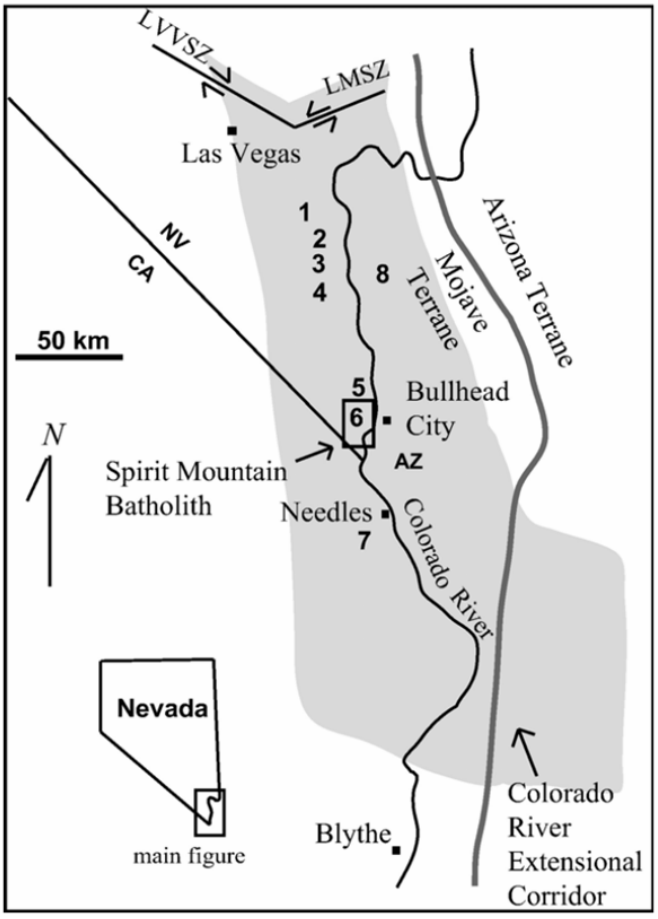


Fig 1. Location map for Spirit Mountain Batholith from Walker et al. (2007). It is one of several Miocene bimodal granite-diorite plutons in southern NV found in the Colorado River Extensional Corridor (highlighted in gray). Miocene plutons: 1– Boulder City; 2 – Nelson; 3 – Aztec Wash; 4 – Searchlight; 6 – Spirit Mountain; 7 – Sacramento; 8 – Mt. Perkins. Cretaceous pluton: 5 – White Rock Wash. LVVSZ – Las Vegas Valley shear zone; LMSZ – Lake Meade shear zone.

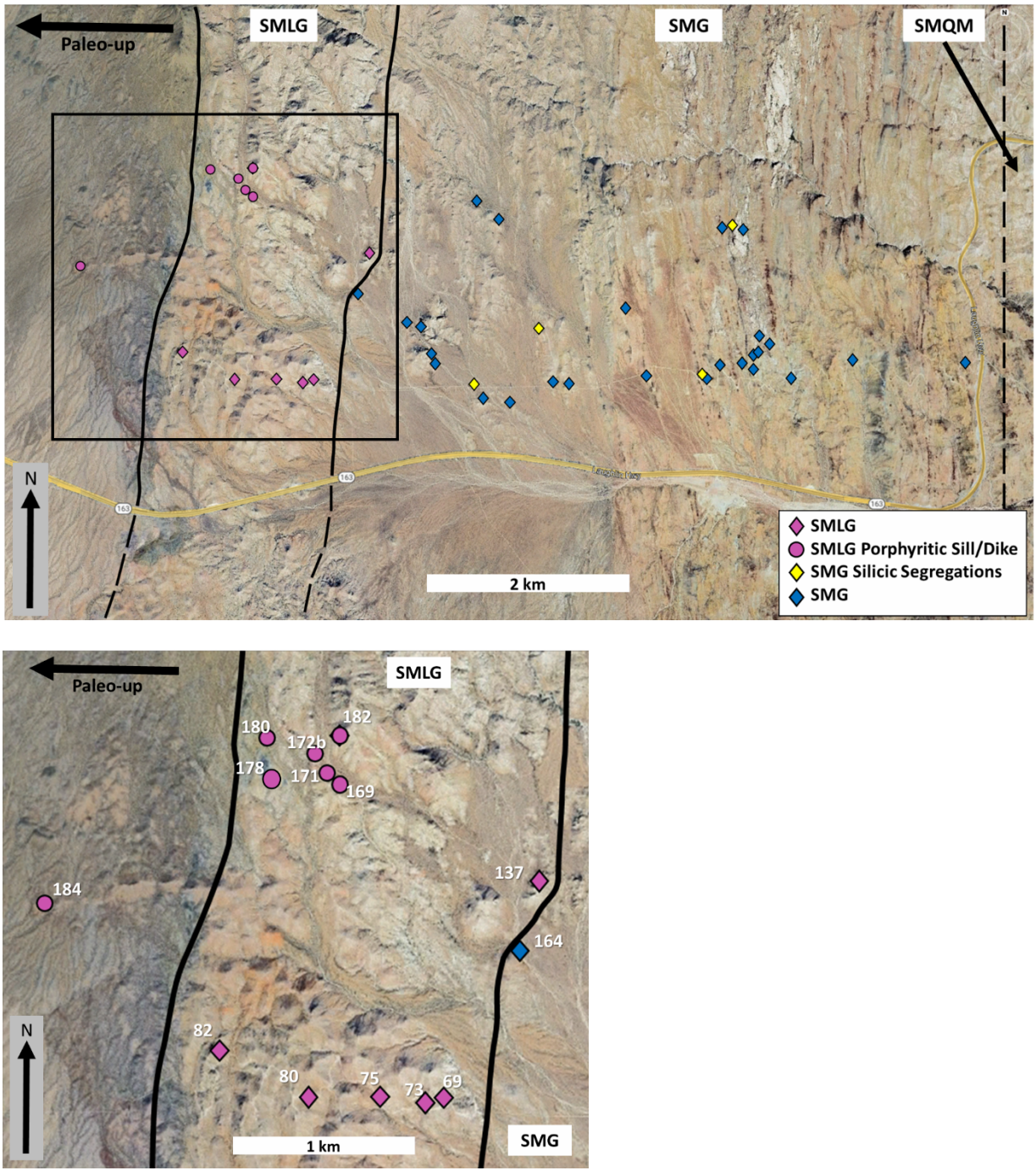


Fig. 2 Google Earth image of Spirit Mountain batholith (inset box from Figure 1). Sample locations from Taylor and Lange (2023) and Taylor et al. (2025) taken along E-W power line road that follows a bottom-top transect through the intrusion. SMLG samples in this study highlighted in pink and labeled within inset box.

SMLG = Spirit Mountain leucogranite, SMG = Spirit Mountain granite, SMQM = Spirit Mountain quartz monzonite.

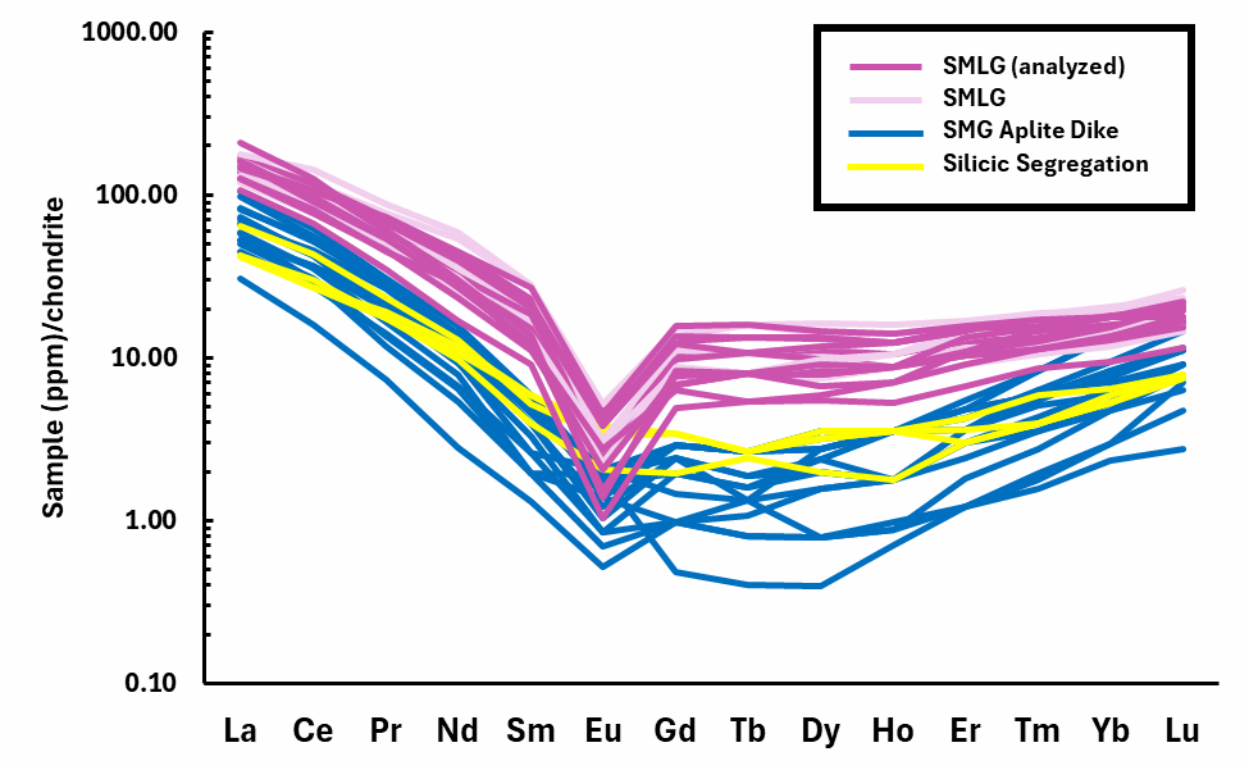


Fig 3. Plot of chondrite-normalized rare-earth elements that compare the horseshoe pattern of the aplite dikes and silicic segregations within the coarse granite with the seagull pattern of the leucogranite cap rocks (Taylor and Lange 2023; Taylor et al., 2025).

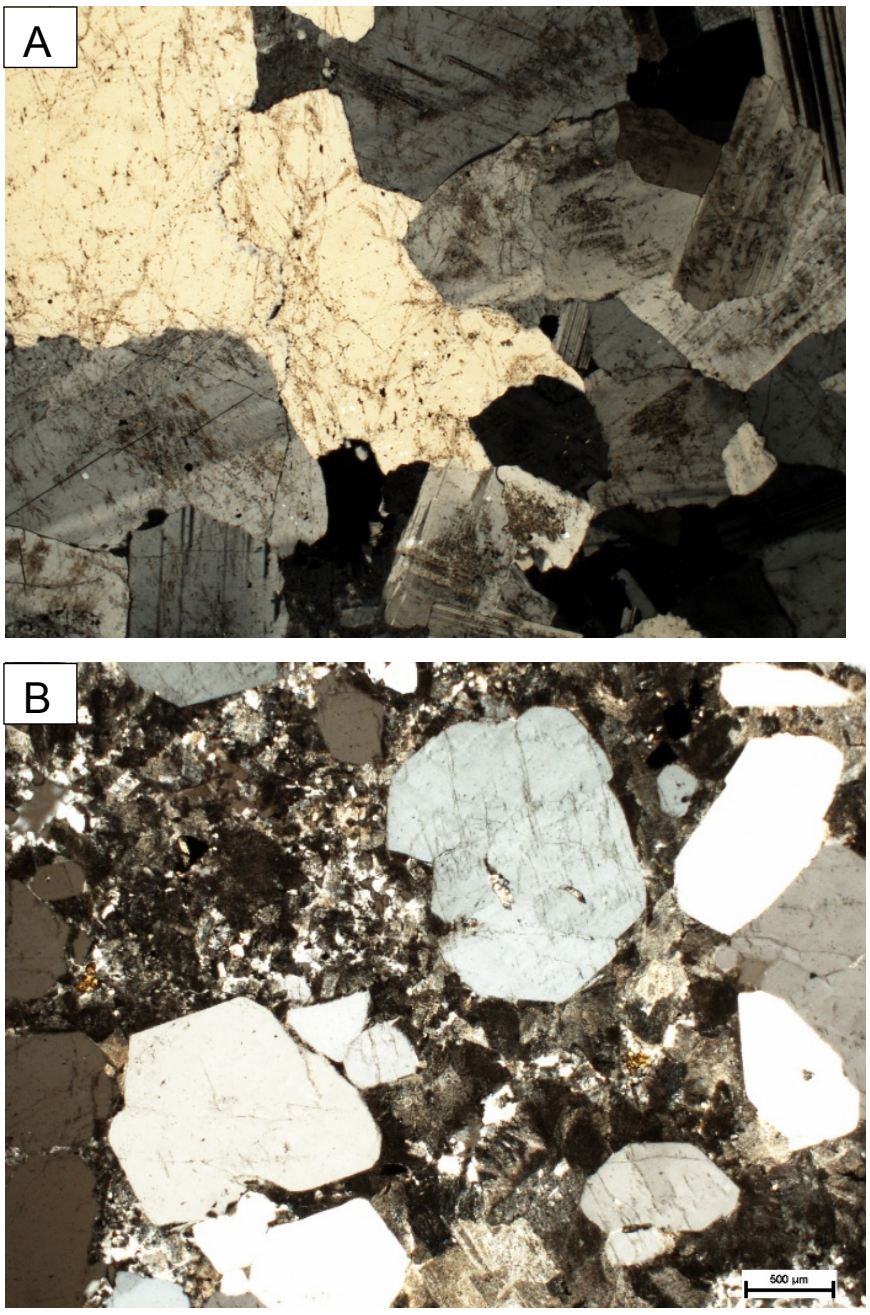


Fig 4. Photomicrographs (crossed-polars) of **(A)** phaneritic leucogranite (SM-73) and **(B)** porphyritic dike (SM-184; ~13 m wide). Field of view is the same in each photomicrograph; scale bar in (B).

A

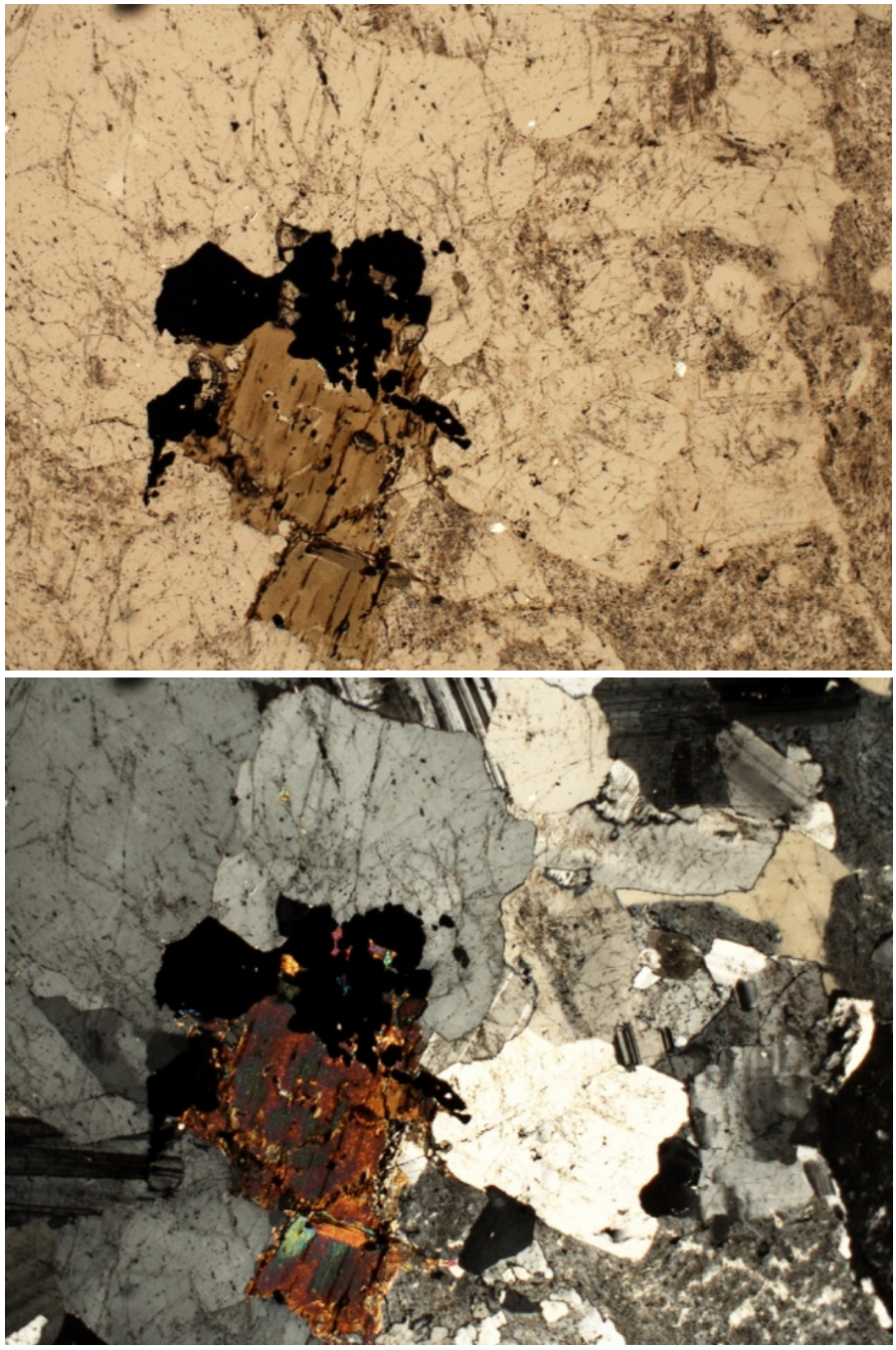


Fig 5. Representative photomicrographs of fresh biotite in SM-73 **(A)** plane polarized light and **(B)** cross-polarized light. Field of view is the same in each photomicrograph in Fig. 4.

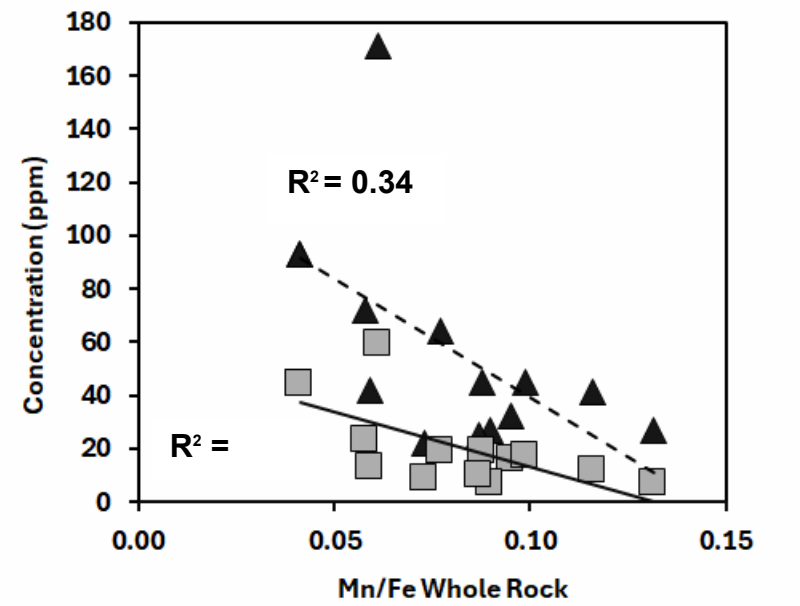


Fig. 6 Plot of whole-rock Mn/Fe ratios vs Sr (gray squares) and Ba (black triangles) ppm. Linear fits show inverse, though relatively weak, correlations. Since decreasing Sr and Ba are markers of increasing differentiation, elevated Mn/Fe ratios broadly reflect degree of differentiation, as previously proposed by Li et al. (2020a).

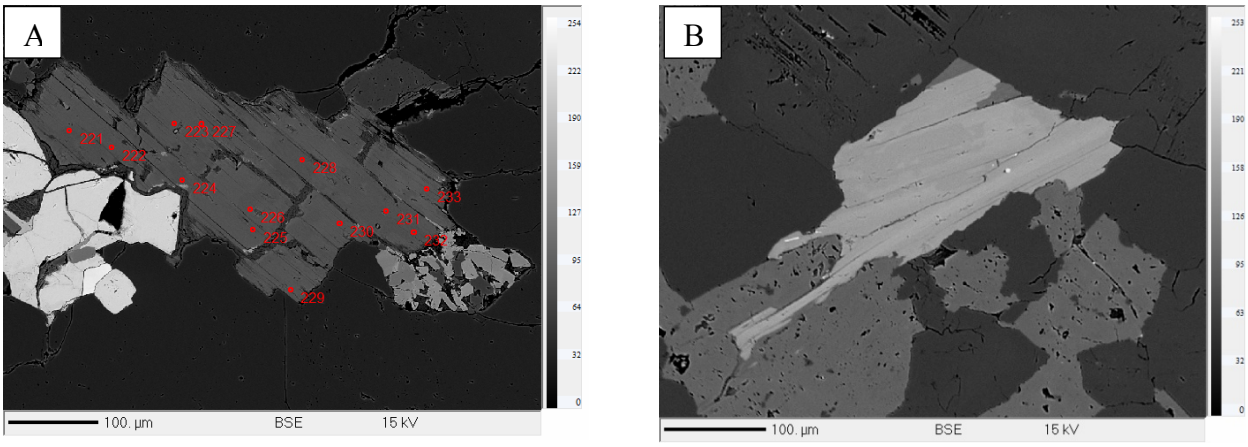


Fig. 7 Representative backscattered electron (BSE) images of fresh biotite crystals in thin sections. (A) SM-137 and (B) SM-171.

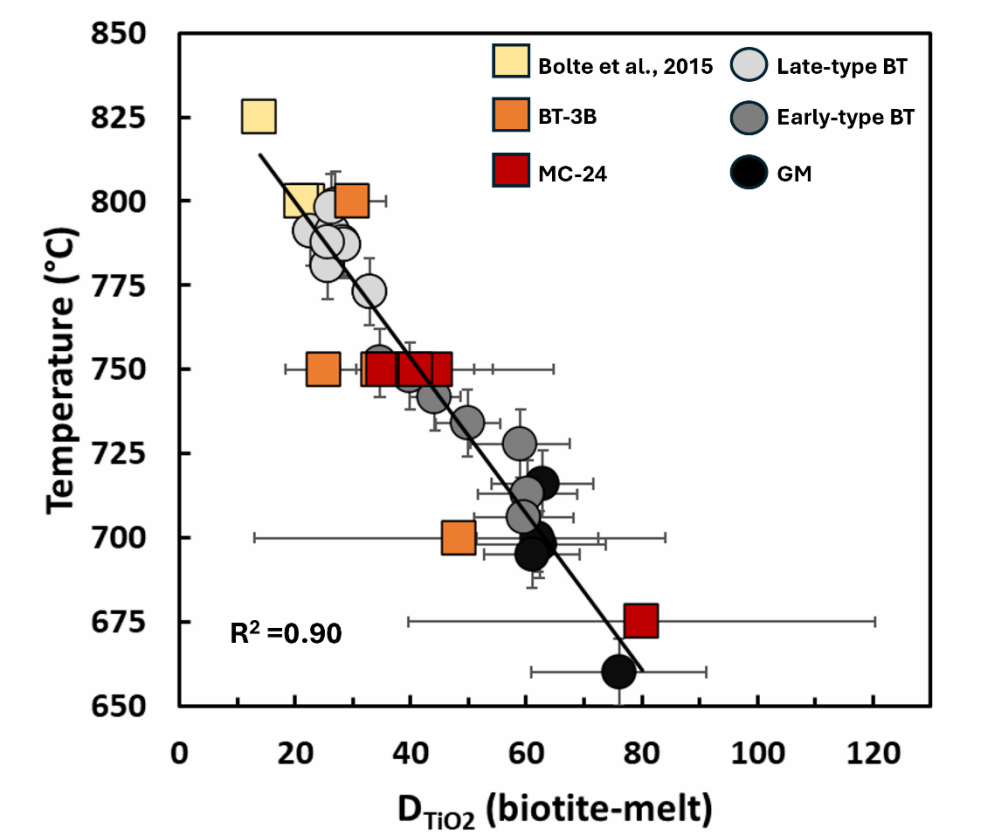


Fig. 8 Plot of temperature vs partition coefficient for TiO_2 between biotite and melt. Natural samples include Early- and Late-type Bishop Tuff samples (Jolles and Lange, 2019) and Glass Mountain samples (Gordon et al, in review). Temperatures are from Fe-Ti oxide thermometry. Also shown are experimental results on Yellowstone HSR (Bolte et al., 2015) and two HSR samples from Gordon et al. (in review), where temperatures are from experimental run conditions. See text for more details.

Fig 9. Analyzed concentrations of TiO_2 (wt%), shown in white, from SM-80 (biotite grain 6; Supplemental Table 2). The results show no clear core to rim zonation pattern in the TiO_2 contents of biotite.

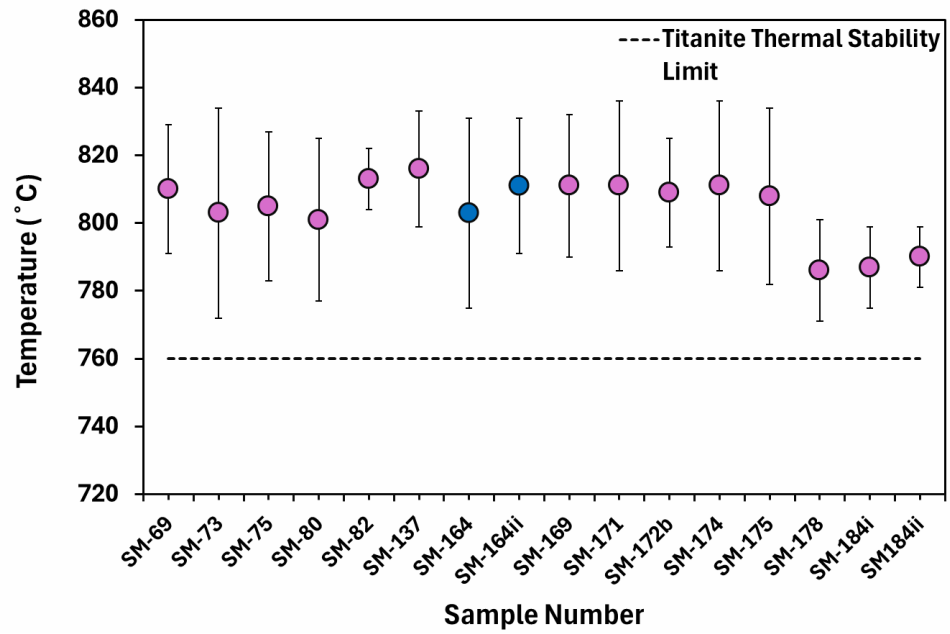


Fig. 10 Plot of average temperature of biotite crystallization for the 13 SMLG (purple) samples and 1 SMG (SM-164, in duplicate; blue) sample. The variance in calculated temperatures is shown by vertical black lines and is propagated from the 3 standard deviation in , which in turn is based on the 3 standard deviation in wt% TiO_2 in the biotite population in each sample. If the range in wt% TiO_2 in the biotite in each sample is due solely to temperature, the entire temperature range of crystallization in each sample is illustrated and ranges from 9-31 °C (Table 3). Since transport from regions of melt segregation to the SMLG cap inevitable involves cooling, these results support melt segregation at temperatures well above the thermal stability limit of titanite (760°C; Colombini et al., 2011) for all samples shown.

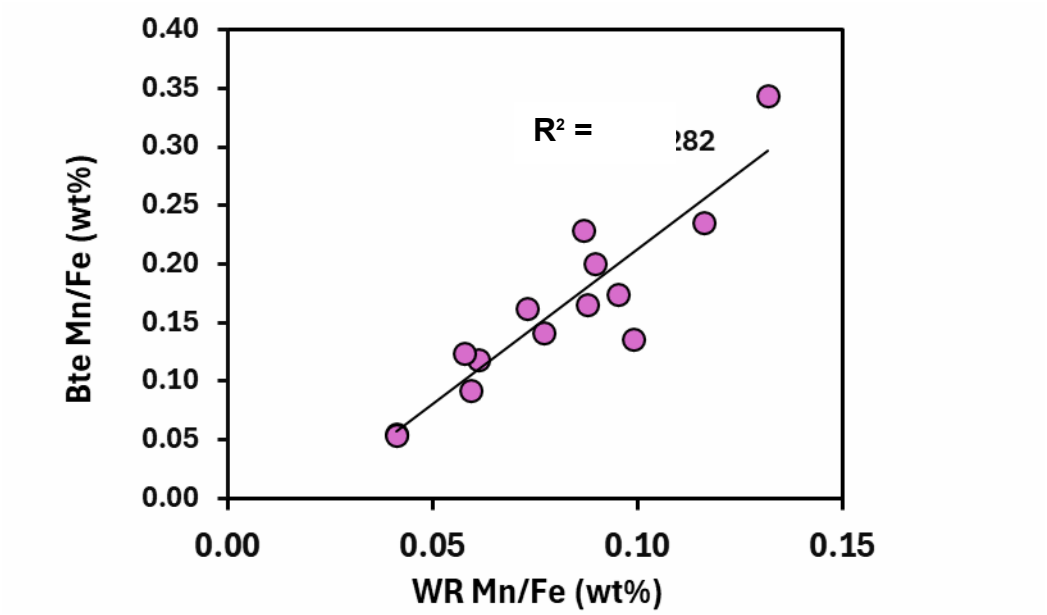


Fig. 11 Plot of Mn/Fe ratios from biotite versus Mn/Fe concentrations in the whole rock for all 13 SMLG samples. The strong linear correlation (R^2=0.83) clearly shows that the remarkably high MnO contents in the biotite crystals in the SMLG samples (Table 2) is due to the elevated Mn/Fe ratios in the whole rock melts from which the biotite crystallized.

Table 1. Analyzed whole-rock compositions of SMLG Cap (normalized to 100%).

Sample	SM-69	SM-73	SM-75	SM-80	SM-82	SM-137	SM-164	SM-169	SM-171	SM-172b	SM-174	SM-175	SM-178	SM-184
Lat. (N 35°)	10.821	10.807	10.824	10.826	10.967	11.47	11.262	35.767	35.787	35.854	35.902	11.902	35.902	35.412
Long. (W 114°)	45.240	45.306	45.476	45.724	46.054	44.879	44.963	45.605	45.605	45.697	45.601	45.601	45.881	46.697
Rock Type	SMLG	SMLG	SMLG	SMLG	SMLG	SMLG	SMG	SMLG Pd	SMLG Pd	SMLG Pd	SMLG Ps	SMLG	SMLG Pd	SMLG Pd
SiO_2 (wt%)	77.75	77.84	78.18	78.47	78.29	76.40	76.01	78.75	77.24	77.34	77.45	78.72	78.45	77.53
TiO_2 (wt%)	0.11	0.10	0.14	0.09	0.10	0.19	0.14	0.09	0.14	0.11	0.10	0.13	0.11	0.13
Al_2O_3 (wt%)	12.37	12.34	11.96	12.10	12.09	12.55	13.44	11.97	12.56	12.66	12.74	11.84	11.90	12.21
FeO_T (wt%)	0.68	0.63	0.81	0.60	0.68	0.98	0.85	0.56	0.69	0.68	0.58	0.65	0.67	0.73
MnO (wt%)	0.06	0.06	0.08	0.07	0.09	0.06	0.03	0.05	0.04	0.05	0.05	0.05	0.04	0.03
MgO (wt%)	0.08	0.09	0.12	0.07	0.07	0.17	0.16	0.05	0.10	0.07	0.07	0.09	0.07	0.08
CaO (wt%)	0.41	0.49	0.45	0.39	0.33	0.57	0.67	0.38	0.43	0.42	0.47	0.38	0.39	0.37
Na_2O (wt%)	3.81	3.95	3.65	3.57	3.95	3.88	3.91	3.90	3.79	3.96	4.20	3.49	3.49	3.52
K_2O (wt%)	4.65	4.43	4.50	4.56	4.32	5.06	4.66	4.19	4.92	4.63	4.28	4.58	4.80	5.28
P_2O_5 (wt%)	0.00	0.00	0.02	0.00	0.00	0.03	0.02	0.00	0.00	0.00	0.00	0.00	0.00	0.03
LOI	1.36	1.39	1.46	1.36	1.54	1.28	1.24	0.70	0.68	0.84	1.01	1.24	0.78	0.89
Total	100.10	98.68	100.10	98.76	100.30	100.50	99.46	100.30	100.50	99.27	99.00	100.90	100.70	99.07
Mg#	0.17	0.20	0.21	0.17	0.15	0.24	0.25	0.14	0.20	0.15	0.18	0.20	0.16	0.16
Mg# w/ Mn	0.16	0.19	0.19	0.16	0.14	0.23	0.24	0.13	0.20	0.15	0.17	0.19	0.15	0.16
Mn/Fe	0.09	0.10	0.10	0.12	0.13	0.06	0.04	0.09	0.06	0.07	0.09	0.08	0.06	0.04
Ba (ppm)	45	32	45	41	27	171	212	27	72	22	25	64	42	93
Sr (ppm)	19	16	17	12	7	59	91	7	23	9	10	19	13	44

SMLG = Spirit Mountain leucogranite, SMG = Spirit Mountain granite

Table 2. Average Analyzed Biotite Composition in Each Sample

Sample (N;n)	SM-69 (7; 25)	SM-73 (9; 67)	SM-75 (8; 32)	SM-80 (13; 60)	SM-82 (4;4)	SM-137 (30; 224)	SM-164i (29; 114)	SM-164ii (17; 89)	SM-169 (9;35)	SM-171 (30;155)	SM-172b (13;58)	SM-174 (20;93)	SM-175 (23;151)	SM-178 (16;76)	SM-184i (6;33)	SM-184ii (5;22)
SiO_2 (wt%)	39.34 (72)	39.08 (89)	38.58 (72)	39.44 (60)	40.14 (76)	38.4 (1.02)	38.14 (1.14)	39.11 (96)	39.93 (64)	38.87 (88)	39.54 (56)	39.47 (69)	39.05 (93)	35.95 (53)	38.49 (54)	38.3 (86)
TiO_2 (wt%)	1.67 (29)	1.84 (46)	2.45 (46)	1.71 (31)	1.37 (12)	2.37 (47)	2.56 (57)	2.08 (42)	1.31 (28)	2.07 (52)	1.72 (26)	1.48 (37)	2.1 (50)	2.81 (22)	3.27 (22)	3.13 (16)
Al_2O_3 (wt%)	12.69 (54)	13.9 (68)	12.73 (47)	15.1 (1.38)	14.76 (63)	12.45 (50)	12.44 (60)	12.00 (50)	16.36 (77)	13.66 (61)	14.78 (91)	15.76 (69)	13.31 (82)	13.1 (36)	12.31 (30)	12.39 (33)
FeO_T (wt%)	14.68 (87)	14.42 (97)	14.6 (90)	14.25 (86)	13.28 (87)	15.65 (1.17)	16.34 (1.40)	15.03 (1.17)	14.06 (87)	15.54 (1.03)	15.15 (73)	13.99 (1.05)	14.89 (99)	22.35 (56)	14.73 (59)	14.69 (71)
MnO (wt%)	2.43 (16)	2.52 (16)	1.98 (31)	3.36 (15)	4.57 (26)	1.86 (16)	1.49 (19)	1.44 (17)	2.82 (36)	1.93 (14)	2.46 (14)	3.21 (71)	2.1 (16)	2.06 (21)	0.81 (03)	0.8 (07)
MgO (wt%)	13.72 (63)	12.34 (84)	13.8 (95)	10.29 (1.57)	9.55 (29)	14.36 (1.05)	13.91 (1.26)	15.03 (1.09)	9.48 (86)	12.36 (82)	10.76 (93)	10.54 (1.00)	13.17 (1.06)	9.05 (52)	16.28 (46)	16.08 (34)
BaO (wt%)	0.02 (02)	0.01 (03)	0.01 (02)	0.01 (03)	0.01 (01)	0.11 (17)	0.13 (20)	0.05 (12)	0.01 (02)	0.07 (18)	0.00 (0.02)	0 (0.02)	0.04 (11)	0.1 (26)	0.08 (13)	0.1 (18)
CaO (wt%)	0.02 (02)	0.01 (02)	0.01 (03)	0.01 (02)	b.d.	0.03 (04)	0.03 (04)	0.04 (05)	0.01 (01)	0.01 (05)	0.01 (02)	0.01 (02)	0.01 (02)	0.05 (05)	0.12 (0.08)	0.13 (09)
Na_2O (wt%)	0.22 (04)	0.24 (05)	0.3 (08)	0.33 (07)	0.36 (01)	0.18 (05)	0.19 (05)	0.19 (04)	0.3 (05)	0.27 (06)	0.27 (06)	0.26 (05)	0.3 (08)	0.13 (02)	0.37 (04)	0.32 (06)
K_2O (wt%)	10.14 (17)	10.14 (17)	10.11 (18)	10.07 (22)	10.14 (20)	10.06 (31)	10.05 (28)	10.13 (25)	10.17 (14)	9.98 (17)	10.16 (19)	10.22 (20)	10.19 (19)	9.44 (24)	9.29 (40)	9.03 (50)
Fe_2O_3 (calc)	6.73	5.20	5.82	4.70	5.43	6.79	6.45	6.54	3.06	5.48	4.39	4.09	5.71	7.66	6.86	6.93
FeO (calc)	8.62	9.74	9.36	10.02	8.39	9.54	10.54	9.15	11.30	10.61	11.20	10.31	9.75	15.46	8.33	8.45
H_2O (calc)	2.86	2.81	2.77	2.62	2.41	2.88	2.91	2.99	2.82	2.87	2.83	2.76	2.83	2.76	2.78	2.79
Total (updated)	99.07	97.83	97.93	97.66	97.13	99.03	98.83	98.74	97.58	98.17	98.12	98.11	98.57	98.57	99.22	98.46
Mg#	0.62	0.62	0.60	0.56	0.61	0.62	0.60	0.64	0.55	0.59	0.56	0.57	0.61	0.42	0.67	0.66
Mg# w/ Mn	0.59	0.59	0.56	0.51	0.57	0.59	0.58	0.62	0.50	0.56	0.52	0.52	0.58	0.40	0.66	0.65
Mn/Fe	0.17	0.17	0.14	0.24	0.34	0.12	0.09	0.10	0.20	0.12	0.16	0.23	0.14	0.09	0.05	0.05
Fe3+/FeT	0.41	0.32	0.36	0.30	0.37	0.39	0.36	0.39	0.20	0.32	0.26	0.26	0.34	0.31	0.42	0.42
T, Si	3.00	2.97	2.94	3.00	3.06	2.91	2.91	2.95	3.02	2.96	3.00	2.98	2.96	2.83	2.88	2.88
T, Al	0.87	0.95	0.93	1.00	0.98	0.93	0.92	0.86	0.99	0.92	0.94	1.03	0.93	0.99	0.97	0.97
T, Fe3_	0.13	0.08	0.12	0.00	0.00	0.15	0.17	0.19	0.00	0.12	0.06	0.00	0.11	0.18	0.15	0.15
sum Tet	4.00	4.00	4.00	4.00	4.04	4.00	4.00	4.00	4.01	4.00	4.00	4.01	4.00	4.00	4.00	4.00
M, Al	0.26	0.29	0.21	0.36	0.35	0.18	0.20	0.21	0.47	0.30	0.38	0.38	0.26	0.23	0.12	0.13
M, Mg	1.55	1.42	1.58	1.20	1.14	1.63	1.59	1.69	1.09	1.42	1.24	1.22	1.50	1.10	1.79	1.77
M, Fe2+	0.54	0.62	0.60	0.64	0.54	0.61	0.67	0.58	0.71	0.67	0.71	0.65	0.62	1.02	0.53	0.53
M, Fe3+	0.25	0.22	0.21	0.27	0.31	0.24	0.20	0.18	0.17	0.19	0.19	0.23	0.21	0.27	0.24	0.24
M, Ti	0.10	0.12	0.15	0.11	0.10	0.14	0.15	0.12	0.09	0.13	0.11	0.10	0.13	0.17	0.18	0.18
M, Cr	0.00	0.00	0.00	0.00	0.00	0.00	0.00	0.00	0.00	0.00	0.00	0.00	0.00	0.00	0.00	0.00
M, Mn	0.15	0.16	0.13	0.22	0.30	0.12	0.10	0.09	0.18	0.12	0.16	0.21	0.13	0.14	0.05	0.05
M, Ni	0.00	0.00	0.00	0.00	0.00	0.00	0.00	0.00	0.00	0.00	0.00	0.00	0.00	0.00	0.00	0.00
M, Li	0.00	0.00	0.00	0.00	0.00	0.00	0.00	0.00	0.00	0.00	0.00	0.00	0.00	0.00	0.00	0.00
Sum Oct	2.85	2.83	2.88	2.79	2.73	2.91	2.90	2.88	2.72	2.84	2.78	2.78	2.86	2.92	2.92	2.91
Oct. Vac	0.15	0.17	0.12	0.21	0.27	0.09	0.10	0.12	0.28	0.16	0.22	0.22	0.14	0.08	0.08	0.09
A, K	1.00	1.01	1.00	1.01	1.04	0.99	0.99	0.99	1.01	0.98	1.00	1.02	1.00	0.98	0.91	0.90
A, Na	0.03	0.04	0.04	0.05	0.05	0.03	0.03	0.03	0.04	0.04	0.04	0.04	0.04	0.02	0.05	0.05
A, Ba	0.00	0.00	0.00	0.00	0.00	0.00	0.00	0.00	0.00	0.00	0.00	0.00	0.00	0.00	0.00	0.00
A, Ca	0.00	0.00	0.00	0.00	0.00	0.00	0.00	0.00	0.00	0.00	0.00	0.00	0.00	0.00	0.01	0.01
Sum inter	1.03	1.04	1.04	1.06	1.09	1.02	1.02	1.02	1.05	1.03	1.04	1.06	1.05	1.00	0.98	0.96
Inter Vacancy	0.00	0.00	0.00	0.00	0.00	0.00	0.00	0.00	0.00	0.00	0.00	0.00	0.00	0.00	0.02	0.04
W, F	0.00	0.00	0.00	0.00	0.00	0.00	0.00	0.00	0.00	0.00	0.00	0.00	0.00	0.00	0.00	0.00
W, Cl	0.00	0.00	0.00	0.00	0.00	0.00	0.00	0.00	0.00	0.00	0.00	0.00	0.00	0.00	0.00	0.00
W, OH	1.44	1.42	1.41	1.33	1.22	1.46	1.48	1.51	1.42	1.45	1.43	1.39	1.43	1.45	1.39	1.40
W, O2-	0.56	0.58	0.59	0.67	0.78	0.54	0.52	0.49	0.58	0.55	0.57	0.61	0.57	0.55	0.61	0.60

Table 3 Biotite-Melt Thermometry Results and Error Propagations

Sample	SM-69	SM-73	SM-75	SM-80	SM-82	SM-137	SM-164i	SM-164ii
Avg Bte wt% TiO_2	1.67	1.84	2.45	1.71	1.37	2.37	2.56	2.08
± 1 s.d.	±0.29	±0.46	±0.46	±0.31	±0.12	±0.47	±0.57	±0.42
± 3 s.d.	±0.87	±1.38	±1.38	±0.93	±0.36	±1.41	±1.71	±1.26
WR wt% TiO_2	0.11	0.10	0.14	0.09	0.10	0.19	0.14	0.14
± 1 s.d.	±0.01	±0.01	±0.01	±0.01	±0.01	±0.01	±0.01	±0.01
Calculated D_{TiO2}	15.18	18.40	17.50	19.00	13.70	12.47	18.25	14.86
± 1 s.d.	±2.98	±4.95	±3.52	±4.04	±1.82	±2.56	±4.28	±3.18
± 3 s.d. (bte only)	±8.03	±13.92	±9.94	±10.55	±3.85	±7.45	±12.28	±9.06
Calculated T (°C)	810	803	805	801	813	816	803	811
± 1 s.d. (and model error)	±9	±13	±10	±11	±8	±9	±12	±10
± 3 s.d. (bte only)	±19	±31	±22	±24	±9	±17	±28	±20

Sample	SM-169	SM-171	SM-172b	SM-174	SM-175	SM-178	SM-184i	SM-184ii
Avg Bte wt% TiO_2	1.31	2.07	1.72	1.48	2.10	2.81	3.27	3.13
± 1 s.d.	±0.28	±0.52	±0.26	±0.37	±0.50	±0.22	±0.22	±0.16
± 3 s.d.	±0.84	±1.56	±0.78	±1.11	±1.50	±0.66	±0.66	±0.48
WR wt% TiO_2	0.09	0.14	0.11	0.10	0.13	0.11	0.13	0.13
± 1 s.d.	±0.01	±0.01	±0.01	±0.01	±0.01	±0.01	±0.01	±0.01
Calculated D_{TiO2}	14.56	14.79	15.63	14.82	16.15	25.55	25.15	24.08
± 1 s.d.	±3.51	±3.86	±2.76	±3.99	±4.04	±3.06	±2.57	±2.22
± 3 s.d. (bte only)	±9.47	±11.19	±7.23	±11.20	±11.61	±6.43	±5.43	±4.13
Calculated T (°C)	811	811	809	811	808	786	787	790
± 1 s.d. (and model error)	±10	±11	±9	±11	±11	±10	±9	±9
± 3 s.d. (bte only)	±21	±25	±16	±25	±26	±15	±12	±9